

Article

# Resolution-Dependent Perspectives on Caribbean Hydro-Climate Change

Mark R. Jury <sup>1,2</sup> 

<sup>1</sup> Department of Physics, University of Puerto Rico Mayaguez, Mayaguez, PR 00681, USA; mark.jury@upr.edu

<sup>2</sup> Department of Geography, University of Zululand, KwaDlangezwa, Richards Bay 3886, South Africa

Received: 20 September 2020; Accepted: 4 November 2020; Published: 28 November 2020



**Abstract:** Near-surface winds around the mountainous Caribbean islands contribute to orographic lifting and thermal diurnal rainfall that requires mesoscale analysis. Here, a new perspective is presented via high-resolution satellite and reanalysis products. Singular value decomposition is applied to 5 km cold-cloud duration satellite data to understand the leading mode of seasonal hydro-climate variability and its regional controls. The spatial loadings reflect wet islands in a dry marine climate, while temporal amplitude is modulated by the large-scale zonal circulation. When summer-time trade winds weaken, daytime confluence around Caribbean islands enlarges, gathering and lifting more moisture. In addition to the static geographic forcing, transient easterly waves impart the majority of marine rainfall between June and September. Higher resolution products capture the thermal orographic effect and reveal upward trends in island rainfall and soil moisture over the satellite era, while lower resolution products miss this effect. The climate of mountainous Caribbean islands is trending toward increased runoff and soil moisture.

**Keywords:** thermal orographic forcing; Caribbean islands; hydro-climate change

## 1. Introduction

Climate change projections over the 21st century show subtropical drying trends that are worrisome for island nations with scarce water supplies [1]. Small islands have greater climate vulnerability due to geographically confined urbanization, reliance on agriculture and tourism, limited internal resources compounded by a decline of expertise, intense storms and prolonged dry spells, declining marine biodiversity, and coastal erosion from rising seas. Coupled models predict that seasonal rainfall in the inter-America subtropics could decrease 30% [2–4] as mean air temperatures rise toward 30 °C encouraging disease transmission. Reductions of greenhouse gas emissions depend on market forces and innovative alternatives that lead to mitigation. In parallel with long-term solutions, well-informed adaptation measures are needed. Engineering our future requires scientific understanding of the immediate climate risks and secondary consequences.

Earlier work on climate change in the Caribbean [5] identified a drying trend attributed to subtropical subsidence from an accelerating Hadley Cell. Concurrently, there was evidence of warming above the boundary layer and a trend for northerly marine winds. However, stream-flows have been rising in many places. This dichotomy means that terrestrial and marine climate regimes should be properly distinguished.

The Caribbean Antilles islands form an arc to the east of Jamaica with a land-sea ratio of ~12% in the domain 15–22 N, 79–58 W. The islands slow the prevailing westward ocean currents and trade winds resulting in surplus heating and warm sea surface temperatures [6]. Orographic effects cause rainfall to be unevenly distributed [7]. Northern slopes receive stratiform showers during winter frontal intrusions, while southern mountains benefit from thunderstorms following summer easterly waves. Dense vegetation and diurnal transpiration stimulate afternoon thunderstorm activity [8,9]

which can double the rainfall from ~900 to 1800 mm/yr [10,11], leading to flash floods within small catchments [12].

Topographic friction and daytime heating initiate convection along shear lines over and around coasts and islands [13–18]. Variations in trade winds alter the width and angle of ‘shadow’ zones and associated cloud bands [19–24]. Most reanalysis and coupled general circulation models under-represent these features over Caribbean islands due to their coarse resolution [25–27]. On the other hand, high resolution models predict that summer thunderstorms will intensify under greenhouse warming [28–30].

The objective of this research is to address the dichotomy of wet islands within a dry zone, featuring a variety of datasets and hydrological outcomes under rising greenhouse gases. Key processes are evaluated using high resolution reanalysis products based on satellite data assimilation. This work is motivated by opposing guidance from coupled model projections for a dry future [31] and observational evidence of moistening trends in the Caribbean.

## 2. Data and Analysis Methods

The Caribbean climate is studied by statistical analysis of rain, wind and weather variables in high-resolution datasets European Centre Medium-Range Weather Forecasts v5 (ECMWFv5) and Hybrid Coordinate Model v3 (HYCOM) underpinned by satellite measurements. Table 1 lists the acronyms, products and references—which cover calibration issues [32–52]. Our target area (15–22 N, 79–58 W, Figure 1a) is a subset of the wider Caribbean, and focuses on the arc of the Antilles islands. The mean annual cycle is calculated for Caribbean winds and rainfall, segregated into land and sea. In addition to maps, vertical cross sections are presented along the trade wind axis (cf. Figure 1b). Soil moisture and runoff data at 10 km resolution are drawn from FEWS Land Data Assimilation System (FLDAS) hydrology reanalysis since 1980. Rainfall is characterized by Climate Hazards InfraRed Precipitation (CHIRP) “cold cloud duration” accumulated from half hourly 5 km geostationary satellite infrared measurements. Its climatology is functionally related to runoff, soil moisture and vegetation fraction (NDVI). The scatterplot (Figure 1c) shows that hydrological variables achieve a Pearson product-moment regression  $r^2 > 0.74$  with CHIRP rainfall at one month lag, suggesting a degree of uncertainty that may be related to resolution or the integrating nature of hydrological responses to rainfall.

A singular value decomposition (SVD) cluster analysis is applied to monthly rainfall records 1981–2019 and the leading mode is extracted. Fields of satellite net outgoing longwave radiation (OLR), sea surface temperature (SST) and reanalysis wind are regressed onto the June–August (JJA) mode-1 rainfall time score over a wide region (10 S–40 N, 130–20 W). The mode-1 score is ranked for wet and dry seasons in the period 1981–2019 (Table 2) and composite difference maps and sections are computed. The time score is correlated with the Southern Oscillation Index (SOI), Pacific Nino3.4 SST, North Atlantic Oscillation (NAO), and Atlantic Multidecadal Oscillation (AMO). Rainfall trends are computed by linear regression 1981–2019 using the 5 km CHIRP reanalysis. Long-term records of Caribbean climate are studied via interpolated insitu data 1950–2019 using Global Precipitation Climatology Centre v8 (GPCC8), Climate Research Unit of UEA v4 (CRU4), ECMWF-20C, and Global Runoff (GRUN) hydrology reanalysis, and placed in context with the AMO via a filter that retains fluctuations >18 months. All acronyms are defined in Table 1 below.

**Table 1.** Datasets used in the analysis.

ACRONYM	NAME	RESOLUTION	SOURCE	REFERENCE
CHIRP	Climate Hazards InfraRed Precipitation (IR-based)	5 km	FEWS via Intl. Res. Inst. Clim.Library	Funk et al., (2014)
CMIP6	Coupled Model Intercomparison Project v6	100+ km	IPCC via Climate Explorer	Eyring et al., (2016)
cMORPH	CPC Morphed precipitation (multi-satellite)	25 km	NOAA via IRI Clim.Library	Joyce et al., (2004)
CRU	Climate Research Unit of UEA v4 (temperature)	50 km	Climate Explorer	Harris et al., (2014)
ECMWF5 EC20C	European Centre Medium-Range Weather Forecasts v5 v20C	25 km 100 km	Climate Explorer	Dee et al., (2011) Poli et al., (2016)
FLDAS	FEWS & Global Land Data Assimilation System v2 (hydrology)	10 km	NASA-giovanni & Climate Explorer	Rodell et al., (2004),
GLDAS		100 km		McNally et al., (2017)
GPCC	Global Precipitation Climatology Centre v8 gauge interpolation	25 km	Climate Explorer	Schneider et al., (2018)
GPCP	Global Precipitation Climatology Precipitation v3 (multi-satellite)	200+ km	NASA via IRI Clim.Library	Huffman et al., (2001)
GPM	Global Precipitation Monitoring (IR+MW multi-satellite)	10 km	NASA-giovanni & Univ.Hawaii APDRC	Huffman et al., (2007) Hou et al., (2014)
GRUN	Global Runoff gauge interpolation	50 km	Climate Explorer	Ghiggi et al., (2019)
HYCOM	Hybrid Coordinate Model v3 Ocean reanalysis	10 km	Univ Hawaii APDRC	Chassignet et al., (2009)
ISIMIP2	Inter-Sectoral Impact Model Intercomparison Project v2 (hydrology)	50 km	Climate Explorer	Frieler et al., (2018)
NASA	National Aeronautics and Space Administration v3 (vegetation)	10 km	IRI Clim.Library	Pinzon and Tucker (2014)
NCEP-2	National Centers for Environmental Prediction v2 reanalysis	180 km	NOAA via IRI Clim.Library	Kanamitsu et al., (2002)
NOAA	National Oceanic & Atmospheric Administration (SST, netOLR)	25–50 km	NOAA via IRI Clim.Library	Reynolds et al., (2007) Lee et al., (2007)
SODA3	Simple Ocean Data Assimilation v3 reanalysis	50 km	UMD via IRI Clim. Library	Carton et al., (2018)
USGS/NWS	River gauge and weather station in Puerto Rico	station	USGS and NWS	waterdata.usgs.gov/pr/nwis/sw Fenton and Keller (2001)

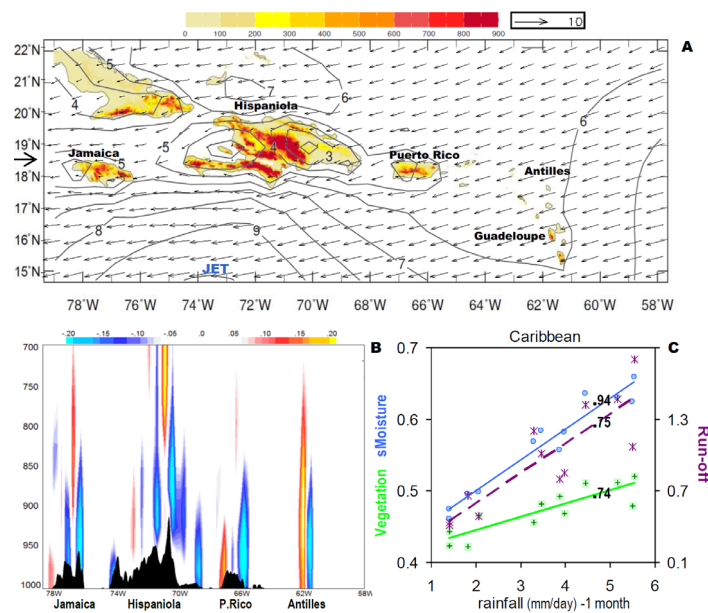


**Figure 1.** (a) Mean ECMWF5 wind vectors, speed isotachs (contour m/s) and topography (shaded). (b) West-east height section of 18–19N averaged EC5 vertical motion (Pa/s, blue upward) with topographic overlay. (c) Scatterplot of (preceding month) island rainfall vs hydrology and their regression ( $r^2$ ).

**Table 2.** Ranked Caribbean wet and dry seasons for SVD composites.

Jun–Aug	Mode 1
<b>wet</b>	<b>mm</b>
2005	21.59
2011	17.93
2010	14.11
2006	9.67
1981	7.68
<b>dry</b>	<b>mm</b>
1982	−6.25
2018	−7.85
1991	−7.90
2015	−8.11
1994	−10.97

A case of strong and weak trade winds is analyzed on 7 June and 10 June 2020 using San Juan radiosonde, 10-km resolution operational winds and Global Precipitation Monitoring (GPM) multi-satellite rainfall over Puerto Rico. Context is provided by computing the mean diurnal cycle of hourly island rainfall and evaporation, and by regression of ECMWFv5 land minus sea rainfall onto evaporation 1979–2019. Satellite vegetation is subjected to SVD analysis and its loading pattern and time score is studied. US Geological Survey (USGS) river discharge data in eastern and western Puerto Rico are analyzed for linear trends 1960–2019.

To analyze the transient part of the Caribbean’s varying climate, easterly waves were identified by coherent propagation in satellite rainfall  $>20$  mm/day and in reanalysis tropospheric winds. Twelve cases (cf. Table 3) were averaged into a composite to study structural evolution and phase speed. The 2–7 day filtered Caribbean marine rainfall is regressed onto the original unfiltered record ( $N = 3652$ ) as a measure of attribution [53]. The filtered record employs three areas spaced progressively at  $5^\circ$  longitude intervals from 60W to 75W over a 3-day period.

**Table 3.** Day-0 of Caribbean easterly waves in the composite analysis.

Year	Month	Day
2010	08	31
2011	08	04
2011	08	23
2012	07	05
2012	08	05
2012	08	24
2014	08	22
2015	08	28
2016	06	20
2016	08	01
2018	06	23
2018	07	10

Lastly, projections of coupled general circulation models (GCM) with the Coupled Model Intercomparison Project v6 (CMIP6) ssp370 moderate greenhouse scenario are extracted for annual Caribbean rainfall and soil moisture using glowb and watergap Inter-Sectoral Impact Model Intercomparison Project (ISIMIP) hydrology sub-models. The moderate scenario generates mid-range warming that is assumed to be most probable. GCM with an incorrect area-average rainfall climatology were screened out, leaving the ‘better’ products as in [1]. Linear trends (mm/yr) and variance ( $r^2$ ) are computed over the period 1950–2050 ( $N = 100$ ). Projections are compared with reanalysis data at various resolutions. Trends for observed values are extrapolated assuming persistence of current climate into the near-future. Reversal of the Atlantic Multi-decadal Oscillation [54] means that extrapolated trends may represent climate change, within bounds of uncertainty [55]. Details on the datasets, acronym, resolution, source, and references are listed in Table 1.

### 3. Results

#### 3.1. Climatology

To understand the Caribbean hydrology, we consider the mean conditions and functional relationships. Surface winds are from 80–90° (Figure 1a) and rise over the mountainous islands creating vertical undulating motions (Figure 1b). Winds < 5 m/s at 19 N contrast with speeds > 9 m/s at 15 N. In Figure 2a the wind rose frequency distribution on Puerto Rico’s east coast illustrates that easterlies are distributed across angles 60–110° at speeds 3–6 m/s. The EC5 reanalysis mean annual cycle (Figure 2b) reveals that Caribbean wind speeds are 3-fold less over land (2.4 m/s) than sea (6.8 m/s). The decile spread is greatest for marine winds in spring and autumn. Caribbean SST (Figure 2c) are modulated by net heat budget and the intrusion of a low saline plume from South American rivers (Figure 2d). Heating of the surface layer occurs downstream from Antilles islands under mean westward currents that vary from 0.02 to 0.07 m/s.

#### 3.2. Rain Modes and Associations

The SVD cluster analysis (Figure 3a,b) offers objective insights on the spatial distribution and temporal frequency of Caribbean rainfall using the high resolution CHIRP product. The 1st mode accounts for 29.3% occurrence ( $r^2$ ), and forms a land/sea pattern indicating that the Antilles islands attract rainfall from the surrounding ocean (Figure 3a). Island ‘footprints’ grow westward in conjunction with geographic size. The 1st mode time score peaks in early and late summer, and wet years are double the amplitude of dry years (Figure 3b). The 2nd mode (not shown) forms a zonal dipole: the eastern Antilles are wet when the western Antilles are dry.

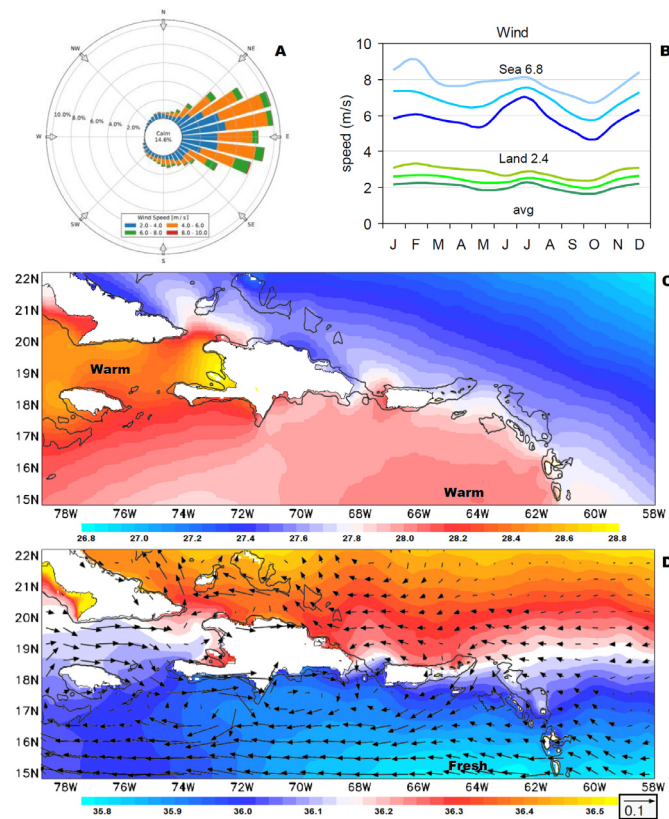


**Figure 2.** (a) Observed wind rose frequency distribution on the east coast of Puerto Rico. (b) Caribbean mean annual cycle and deciles of ECMWF5 surface wind speed over sea and land. HYCOM climatology of: (c) SST (°C) and, (d) surface salinity (ppt) and currents (vector); including 500 m depth contour.

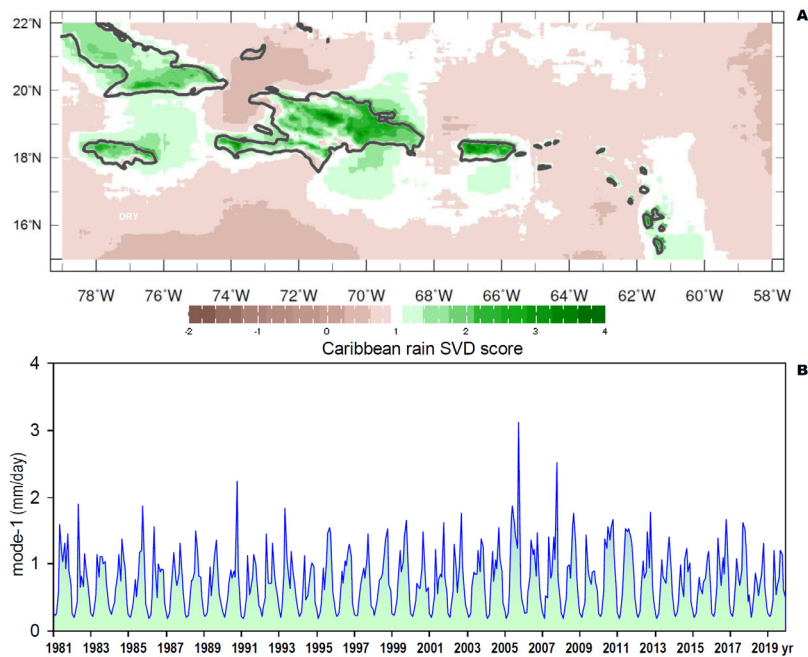


**Figure 3.** (a) Loading map for SVD mode-1 CHIRP rainfall and (b) its associated mode-1 time score.

Regional drivers of mode-1 rainfall are analyzed in Figure 4a–c. The 1st mode (JJA-season) regression onto the regional net OLR field demonstrates convection across the Caribbean basin and

opposing (dry) conditions and cool SST in the subtropical North Pacific (Figure 4a). Caribbean rainfall is enhanced by warmer SST in the tropical Atlantic (15°N, Figure 4b), where easterly waves entrain moisture. There is a large scale weakening of low-level easterly flow associated with mode-1 rainfall (Figure 4c) that spreads zonally from Central America. Mode-2 (not shown) is forced by a Rossby wave-train, whose trough-ridge patterns shift rainfall east-west across the Caribbean (Hernandez-Ayala 2019). Summer rainfall over the Antilles islands is favored by weak trade winds, evident in the composite wet-dry differences (Figure 5a,b), as part of a wider Pacific-Atlantic circulation (Wang 2004) that imparts easterly shear. As the Caribbean Current weakens (Figure 5c), the longer residence time under surplus heating leads to higher SST and a warm moist air mass.

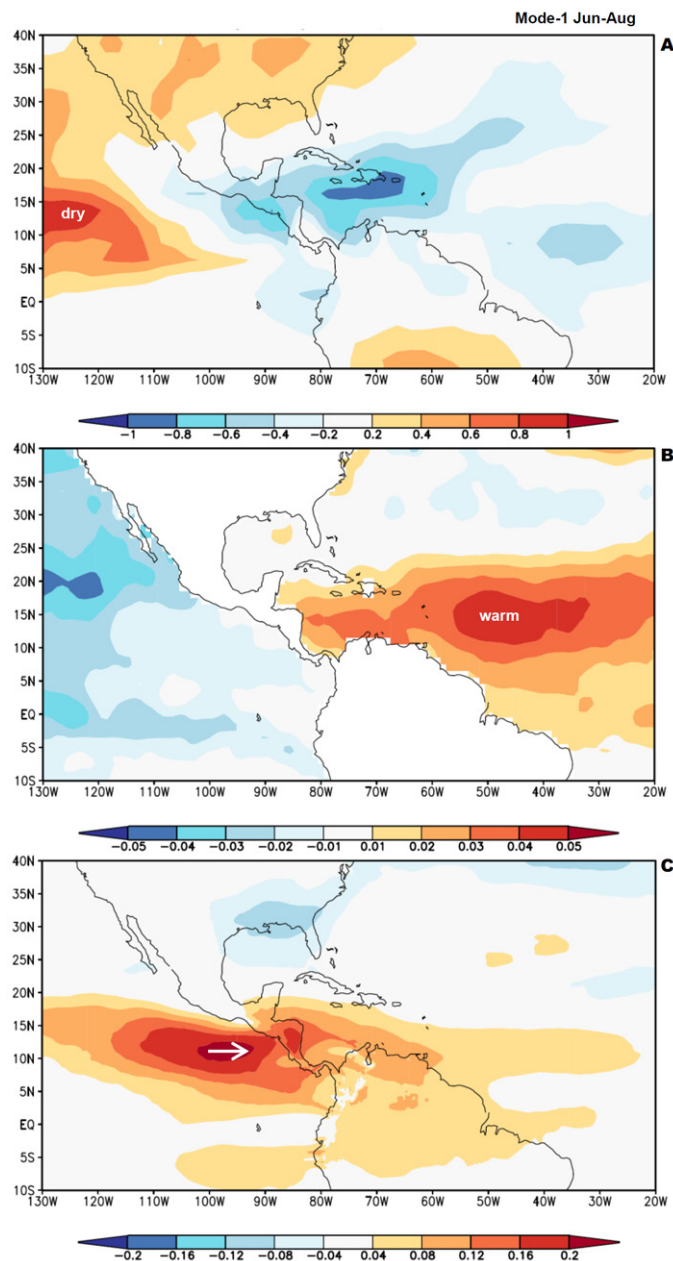


**Figure 4.** Regression of SVD time score for rain mode-1 Jun-Aug onto fields of: (a) net OLR (W/m<sup>2</sup>), (b) SST (°C), and (c) 700 hPa zonal wind (m/s).

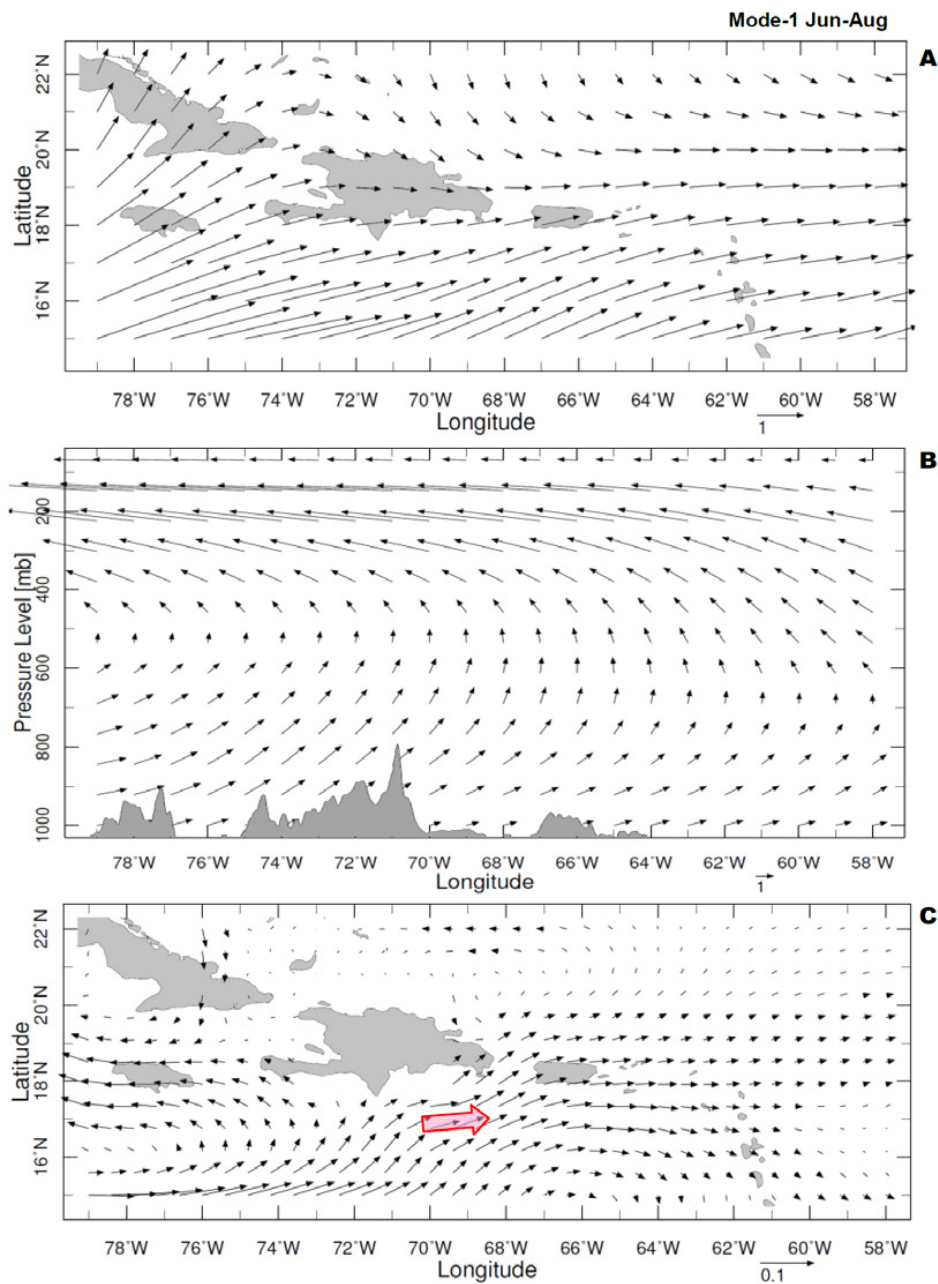


**Figure 5.** Composite wet minus dry differences in: (a) surface winds, (b) vertical cross section of zonal circulation, and (c) near-surface currents, with anomaly highlighted. Based on seasons listed in Table 2.

The Caribbean rainfall mode-1 time score is weakly related with Pacific Nino3.4 SST and NAO, however potential multi-decadal influences from the AMO guide us to longer records for evaluation of climate change (Figure 6a). Only the CRU4 temperature has a significant trend  $0.014\text{ }^{\circ}\text{C}/\text{yr}$  with  $r^2 = 0.79$  (18-month filtered). EC20C winds, GPCC8 rainfall and GRUN runoff averaged over the Caribbean since 1950 exhibit oscillations of 3, 6, 9 year period. The AMO influence on Caribbean run-off is weak, evident by comparison in Figure 6a lower.

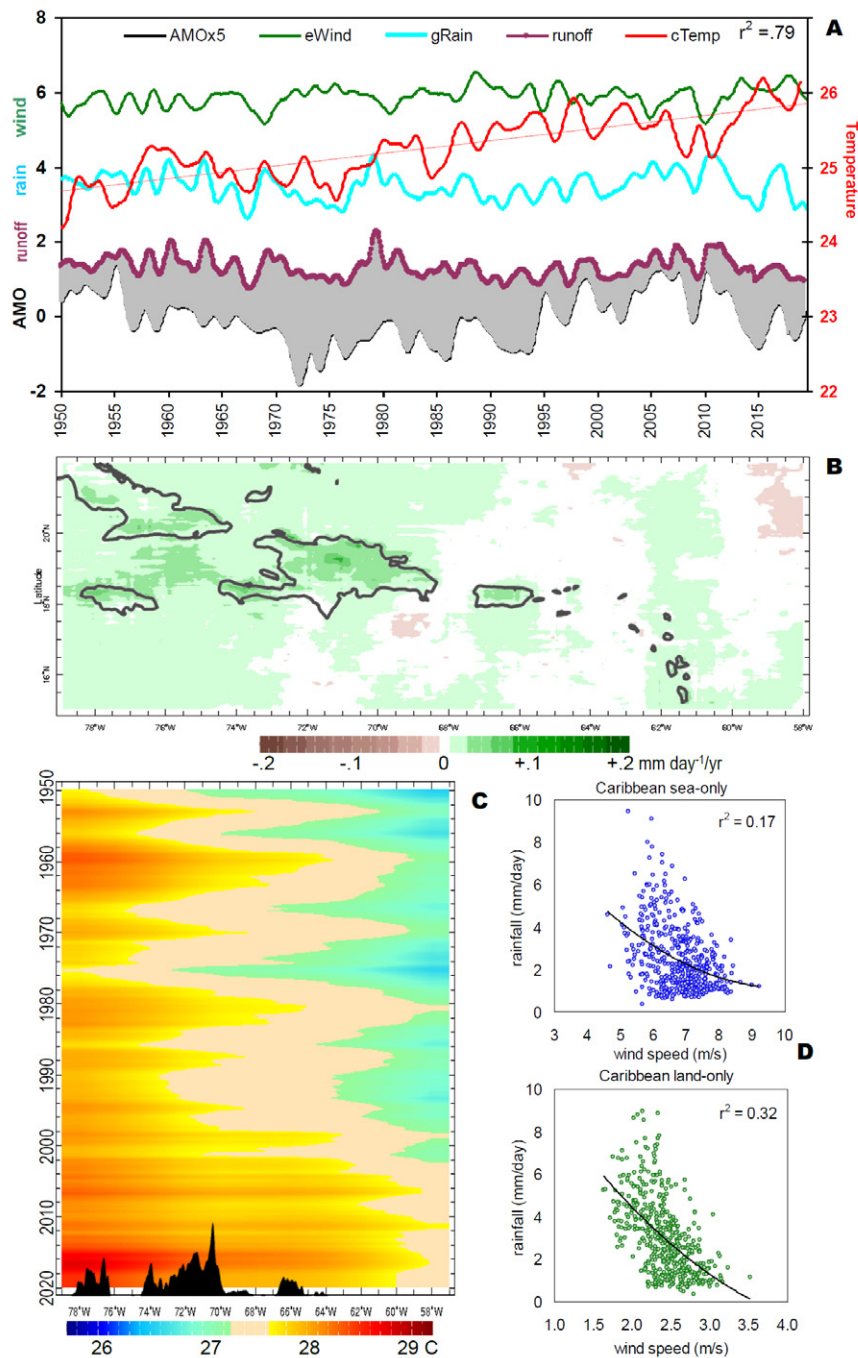


**Figure 6.** (a) Long-term records of 18-month filtered Caribbean climate; shading (lower) highlights weak AMO influence on runoff; trends are significant for air temperature (cTemp). (b) CHIRP rain trend analysis 1981–2019 ( $\text{mm day}^{-1}/\text{yr}$ ). (c) NOAA SST hovmoller plot avg 15–22° N highlighting eastward expansion of the Atlantic warm pool since 1950, with topography lower. (d) Temporal scatterplots of monthly Caribbean ECMWF5 wind speed vs rainfall for sea and land 1979–2019 ( $N = 480$ ).

The spatial structure of CHIRP rainfall trends in the satellite era (Figure 6b) is distinctly positive over the Antilles islands. Trends over the sea are weakly positive, consistent with eastward expansion of the Atlantic warm pool (Figure 6c). A longer fetch for trade winds over SST  $> 28$  °C moistens the boundary layer downstream. Segregating the EC5 rain and wind over sea and land, an inverse relationship is evident in scatterplots (Figure 6d). Stronger trade winds suppress rainfall moreso

over land ( $r^2 = 0.32$ ). On the other hand, lighter trade winds and associated surplus heating underlie easterly shear (cf. Figure 5b) and enhanced rainfall.

### 3.3. Geographic Forcing

Many characteristics of Caribbean hydro-climate have been described, but the way that Antilles islands “attract” rainfall is obscure. Thermal orographic processes are prevalent, but how do they function? A case study of strong vs weak trade winds over Puerto Rico is presented in Figure 7a,b. The radiosonde profile confirms that moist instability ( $\Theta_e$ ) is similar in both cases, but that boundary layer winds are 15–20 kt on 7 June vs. 5–8 kt on 10 June 2020. The afternoon wind convergence onto the island covers a wider area in the weak case and daily rainfall of  $>10$  mm extends  $50 \times 100$  km<sup>2</sup> (cf. Figure 7b), yielding a volume of  $50$  M m<sup>3</sup> attributable to transpiration and seabreezes, rather than synoptic weather forcing. Peak discharge at the Añasco River flow gauge doubled to  $178$  m<sup>3</sup>/s under weaker winds. Both days had precipitable water of 43 mm and convective available potential energy  $>1000$  J/kg at the upstream radiosonde station. Transpiration over the island yields  $\sim 25$  M m<sup>3</sup> of moisture, so additional marine evaporation of  $\sim 25$  M m<sup>3</sup> is needed to supply the precipitation volume. This comes from the nearshore zone where afternoon trade winds turn landward.

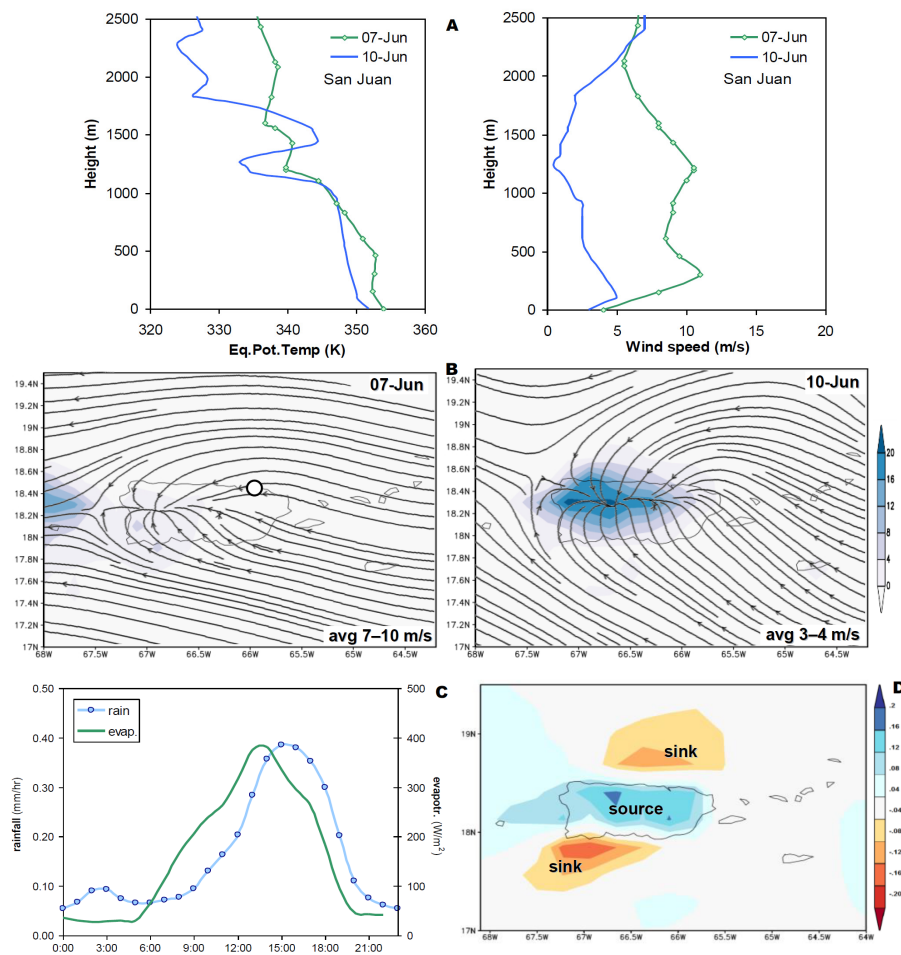


**Figure 7.** Strong vs weak trade wind case study: (a) San Juan radiosonde profiles (at dot in b) comparing equivalent potential temperature (left) and wind speed (right). (b) Operational wind streamlines at 2 pm and daily GPM rainfall (mm) for 7 June (left) and 10 June (right). (c) Mean diurnal cycle of rainfall and evapotranspiration over the island. (d) 1979–2019 regression of annual land minus sea rainfall onto ECMWF5 evaporation, positive upward.

The diurnal climatology analyzed in Figure 7c suggests that ~50% of rainfall is attributable to the thermal orographic effect in Puerto Rico (e.g., land–sea contrasts in potential temperature). The mean evapotranspiration rises during the day to a peak of 380 W/m<sup>2</sup> at 14:00, followed by rainfall up to 0.4 mm/h at 16:00 local time, a process that occurs over other Antilles islands. Correlating the land minus sea rainfall over Puerto Rico with EC5 evaporation 1979–2019, the island footprint emerges in Figure 7d. Transpiration over the island is a source of moisture, while areas north and south of the island are ‘sinks’ where trade winds deflect landward in the afternoon.

Diurnal transpiration derives from vegetation cover, as analyzed in Figure 8a,b via SVD. The leading mode shows positive loading over windward portions of Caribbean islands, and a time score with annual cycle and weak rising trend  $r^2 = 0.09$ . We attribute the greening to increased carbon dioxide concentrations [56] and urban migration that preserves hinterland cover. In consequence of trade wind moisture uptake over the islands, river discharge on the western side is rising while eastern catchments show steady flows (Figure 8c). The background trend is relatively small compared with the seasonal cycle and storm events. Soil moisture from FLDAS reanalysis exhibits upward trends in the satellite era of ~0.05% y<sup>-1</sup> over most islands (Figure 8d); only the small flat islands and eastern sides (Hispaniola) have weak downward trends. Trade wind uptake of diurnal transpiration underpins Antilles island moisture supply, and could accelerate with rising greenhouse gases.

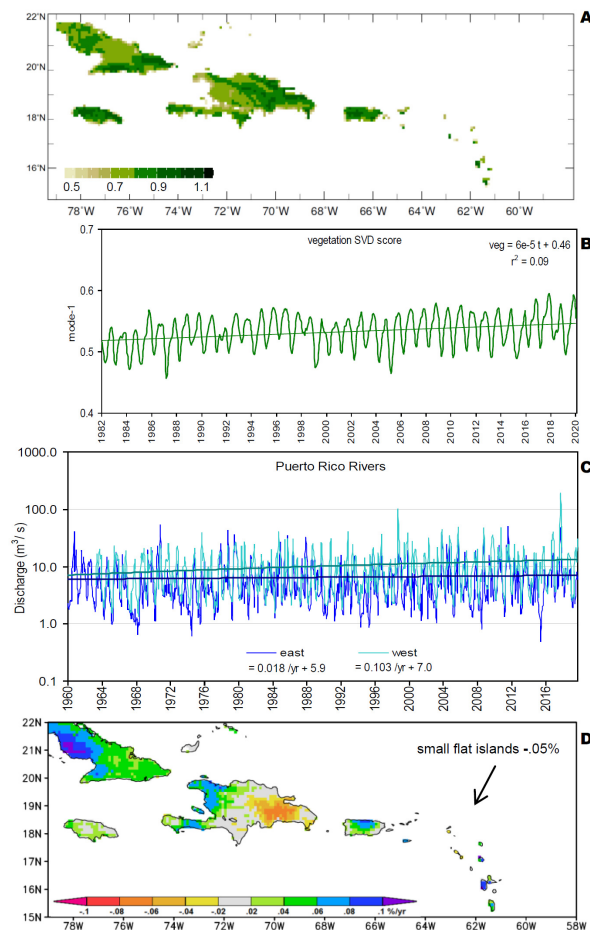


**Figure 8.** NASA satellite vegetation (color) fraction SVD mode-1: (a) loading pattern and (b) time score with trend. (c) Observed Puerto Rico river discharge in eastern (Loiza) and western (Anasco) catchments and linear trends, (gauges shown in Figure 10d). (d) FLDAS soil moisture trend 1981–2019 (% y<sup>-1</sup>).

### 3.4. Transient Weather Processes

The SVD analysis has resolved the static features of Caribbean climate associated mainly with land-sea distribution. Next, we analyze the transient evolution of a composite easterly wave in Figure 9. Wave-induced convection shifts westward at  $\sim 6.2$  m/s over a 3-day period. Southeasterly flow behind the trough is 2x stronger than the northeasterly flow in front, indicative of a circulation that gains planetary vorticity according to the simplified equation:  $W = V(\Delta Z)(\beta/f)$ . Given a southerly wind  $V \sim 5$  m/s, atmospheric thickness  $\Delta Z \sim 5 \times 10^3$  m,  $\beta = df/dy \sim 2 \times 10^{-11} \text{ s}^{-1}$  for flow oscillating from  $15^\circ$ – $22^\circ$  N, and  $f \sim 5 \times 10^{-5} \text{ s}^{-1}$ , the outcome is  $W = 10^{-2} \text{ m s}^{-1}$ . Hence, rising motions occur within airflow from the southeastern Caribbean, where South American river plumes contribute to surface warming (cf. Figure 2c,d). In the Jun-Sep season, over two-thirds ( $r^2 = 0.68$ ) of marine rainfall is derived from transient easterly waves of 2–7 day period.

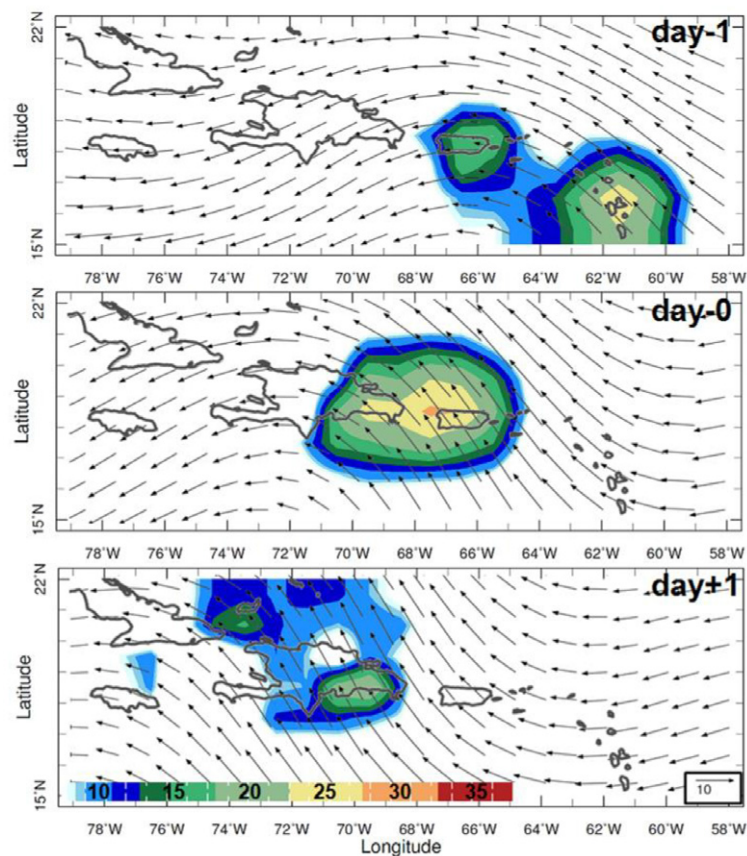


**Figure 9.** Maps of composite easterly wave rainfall (mm/day) and 1000–500 hPa layer winds over a 3-day period (top-down) with scales in the lower panel; based on dates in Table 3.

### 3.5. Resolution Dependent Outcomes

The mean annual cycle of Caribbean rainfall is analyzed in Figure 10a,b at varying resolution and associated land-sea ratio. The maps at left dramatize how the Antilles Islands ‘sink into the sea’ as resolution declines from 5 to 200 km. The eastern arc of islands and shelf that is fully resolved at 5 km, is partially evident at 25–100 km, and completely missing at 200 km resolution. The CMIP6 cGCM and 200 km GPCP satellite products simulate less rain (Figure 10b, compare with [1]), only reaching 2–4 mm/day in May/June, Sep–Oct. In contrast, island rainfall measured by 5–25 km satellite and reanalysis products exceeds 5 mm/day in May, Sep–Oct, with representative surface forcing.

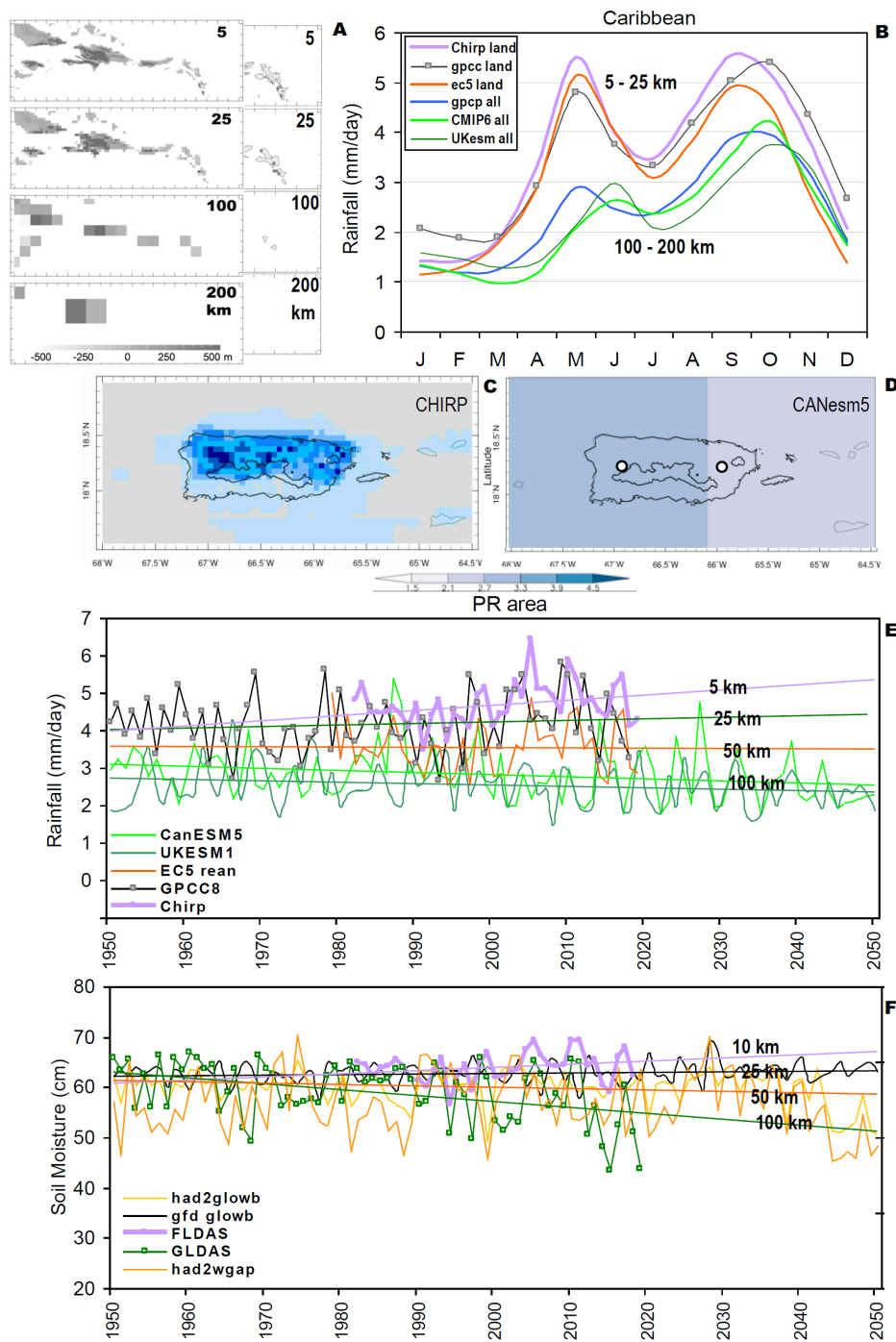


**Figure 10.** (a) Shelf and island topography at resolution from 5–200 km (shaded light to dark grey –500 to 500 m elv). (b) Mean annual cycle (1980–2019) of land-only and all Caribbean rainfall per dataset. Comparison of mean pattern of annual rainfall: (c) CHIRP and (d) cGCM (mm/day). Time series and trends over Puerto Rico in observed and model datasets with resolution labeled: (e) rainfall, and (f) soil moisture. Trends for observed values are extrapolated into the future assuming persistence. River discharge (cf. Figure 8c) at dots in d) above.

Maps of mean rainfall over Puerto Rico are illustrated using 5 km CHIRP and 100 km CMIP6 cGCM products. The model simulates a westward increase but no thermal orographic ‘footprint’ (Figure 10c,d). Time series of fine resolution products reflect more rain and upward trends (Figure 10e),

whereas the (few) CMIP6 models with grid points over the island, simulate less rain and downward trends. Thus trends are resolution-dependent, and appear to “fan-out” in the future.

Although soil moisture is modulated by mean rainfall and evaporation (latent heat flux), the conversion to runoff is controlled by land cover, terrain slope and soil characteristics (cf. Figure 1c). These factors are incorporated into hydrological data assimilation and ISIMIP2 models, and reveal a similar tendency for moistening at fine resolution (Figure 10f, e.g., FLDAS 10 km) compared with drying at coarse resolution.

#### 4. Concluding Discussion

This work has sought to define mesoscale features and processes of Caribbean hydro-climate, and in so doing, has found that resolution makes a difference. The two key problems at coarse resolution: (i) the eastern arc of the Antilles islands “sink into the sea”—permitting unrealistic currents and SST, and (ii) thermal diurnal and orographic forced uplift can not develop without mountainous islands. Figure 10a illustrated these attributes in a sequence of maps at resolutions degraded from 5 to 200 km. Yet coarse resolution GCM may be valuable for marine climate, provided they are screened for potential bias. Here, observed and projected values for rainfall were compared in a 40 y overlap period (cf. Figure 10b), which directed effort toward GCM with better simulated rainfall climatology. Although feedbacks between rainfall, vegetation, soil moisture and runoff have uncertainty (cf. Figure 1c), coupled data assimilation should offer insights on mesoscale processes linking trends in land, sea and air.

Using climatology and statistical analysis applied to high resolution reanalysis data, key processes underlying Caribbean rainfall were isolated. The westward increase of SST and convection [6] derives from a net heat budget surplus of  $10.6 \text{ W/m}^2$  that peaks in early summer. Westward surface ocean currents alter residence times from 3 to 9 months in dry vs wet years. The regression of SST onto mode-1 summer rainfall revealed a warm zone southeast of the Antilles islands (cf. Figure 4b). A case study contrasting strong vs weak trade winds over Puerto Rico found an additional moisture flux of  $\sim 25 \text{ M m}^3$  due to seabreeze convergence. The larger island footprint and greater diurnal inflow supports cloud bands in mid-summer. This seasonal focus was intentional, given the influence of Jun-Aug dry spells on hydrological budgets [57].

Past studies using coupled models have projected a  $0.3 \text{ m/s}$  increase in trade winds and a  $\sim 20\%$  decline in rainfall [58]; their Figure 7k and Figure 9 leading to a depletion of Antilles island soil moisture [31]; their Figures 20.4, 20.7. In contrast, weak upward trends in streamflow observations and 5–10 km resolution moisture reanalyses have been documented here. Longer records suggest steady hydrological outputs across the Caribbean, notwithstanding multi-decadal oscillations. Rising  $\text{CO}_2$  concentrations may stimulate thermal orographic rainfall (diurnal cloud bands) over Antilles islands, causing western rivers to flow more than eastern (cf. Figure 8c). Moisture convergence depends on land-sea gradients that enlarge under weaker trade winds (cf. Figure 7b). The mid-level sinking / drying reported in earlier work [1,2,59] is absent in modern EC5 reanalysis (cf. Appendix A Figure A1). Instead there is rising / moistening above the Caribbean low level jet and temperatures over Antilles islands are warming faster than the surrounding sea. Understanding hydro-climate change in the Caribbean requires 5–10 km resolution.

Appendix A Figure A2 illustrates field-to-field scatterplots of mode-1 spatial loadings (cf. Figure 3a) onto elevation (Figure 1a), SST (Figure 2b), vegetation fraction (Figure 8a) and longitude, mapped at 5 km resolution. These represent spatial associations in a domain with 12% land ( $N = 59360$ ) and multivariate forcing of rainfall by transpiration over mountainous islands within a background westward increase due to SST and currents. Mesoscale thermal orographic processes are embedded in a zonal overturning circulation that spans the Pacific-Atlantic (cf. Figure 5b) involving the Caribbean low-level jet. Secondary consequences of weaker trade winds include sluggish currents, locally warmer SST, more moisture, and easterly wind shear that sustains tropical waves in mid-summer.

Based on persistence forecasts extrapolated from fine scale observations over the satellite era, the future climate of mountainous Caribbean islands appears headed toward increased rainfall, soil moisture and runoff (cf. Figure 10e,f) within bounds of uncertainty. Small flat islands and southeast coasts of larger islands (cf. Figure 8d) may not share the benefits of diurnal cloud bands, instead they depend on transient marine rainfall which may decline in future [26,31,58]. Although we have resolved thermal orographic footprints around the Antilles islands and observed how diurnal processes contribute to hydro-climate outcomes, periodic drought will require water engineering to alleviate wastage between supply and demand, underpinned by local government systems to generate and utilize revenue in an equitable manner.

**Funding:** This research received no specific external funding.

**Acknowledgments:** The suppliers of data and analysis tools employed here (cf. Table 1) are acknowledged. José J. Hernández-Ayala of Sonoma State University gave useful feedback on the paper. On-going support from the S.Afr. Dept of Education is recognized.

**Conflicts of Interest:** The author declares no conflict of interest.

### Appendix A

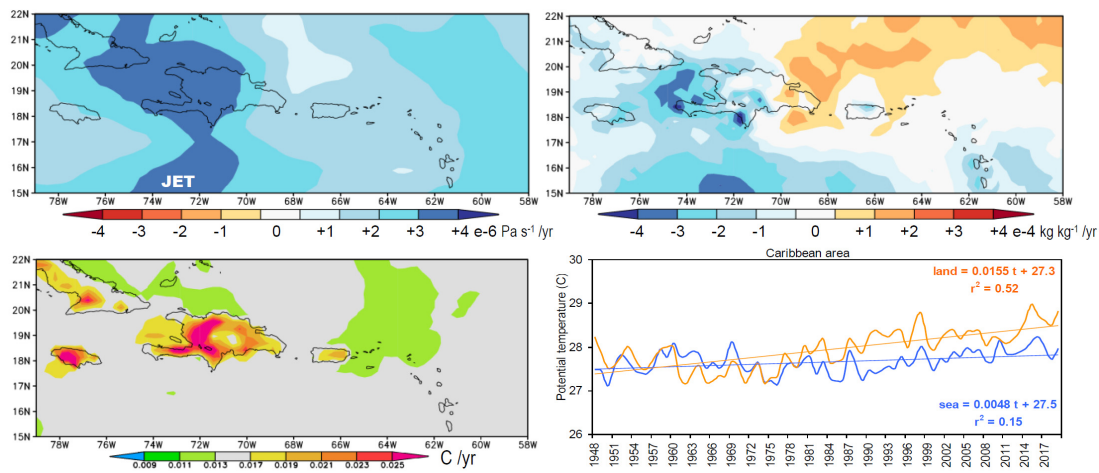


**Figure A1.** Trend analysis of ECWMF5: (top row) 500 hPa vertical motion and specific humidity, blue upward moistening; (lower row) surface air temperature and annual time series over land and sea.

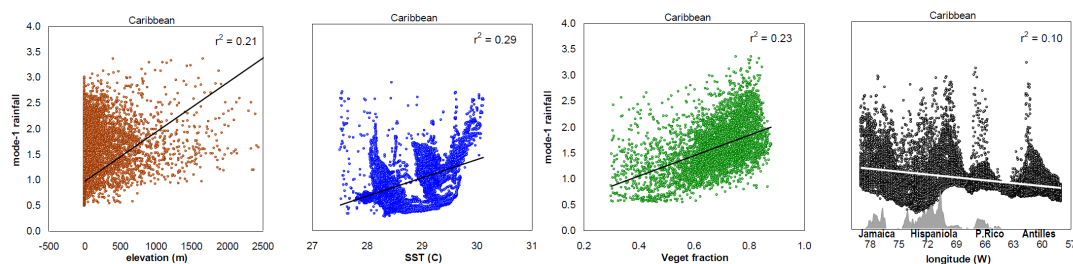


**Figure A2.** Spatial scatterplots of field-to-field rainfall (cf. Figure 3a) and (left-to-right): elevation (Figure 1a), SST (Figure 2c), vegetation (Figure 8a), and longitude, with topographic profile lower, and linear regression. At 5 km resolution, the Caribbean field matrix is 59360 with 7182 pixels above sea level (e.g., land).

## References

1. Taylor, M.A.; Clarke, L.A.; Centella, A.; Bezanilla, A.; Stephenson, T.S.; Jones, J.J.; Campbell, J.D.; Vichot, A.; Charlery, J. Future Caribbean climates in a world of rising temperatures: The 1.5 vs 2.0 dilemma. *J. Climate* **2018**, *31*, 2907–2926. [[CrossRef](#)]
2. Campbell, J.D.; Taylor, M.A.; Stephenson, T.S.; Watson, R.A.; Whyte, F.S. Future climate of the Caribbean from a regional climate model. *Int. J. Climatol.* **2011**, *31*, 1866–1878. [[CrossRef](#)]
3. Karmalkar, A.V.; Taylor, M.A.; Campbell, J.; Stephenson, T.; New, M.; Centella, A.; Bezanilla, A.; Charlery, J. A review of observed and projected changes in climate for the islands in the Caribbean. *Atmósfera* **2013**, *26*, 283–309. [[CrossRef](#)]
4. Ryu, J.-H.; Hayhoe, K.K. Understanding the sources of Caribbean precipitation biases in CMIP3 and CMIP5 simulations. *Climate Dyn.* **2014**, *42*, 3233–3252. [[CrossRef](#)]
5. Jury, M.R. The pattern of climate change around the Windward Passage. *Theor. Appl. Climatol.* **2018**, *134*, 1–9. [[CrossRef](#)]
6. Jury, M.R. Zonal gradients in the lower atmosphere and upper ocean across Puerto Rico and the windward Antilles in mid-summer 2012. *J. Appl. Meteor. Clim.* **2013**, *53*, 731–741. [[CrossRef](#)]
7. Hernández-Ayala, J.J.; Keellings, D.; Waylen, P.R.; Matyas, C.J. Extreme floods and their relationship with tropical cyclones in Puerto Rico. *Hydrol. Sci. J.* **2017**. [[CrossRef](#)]
8. Malkus, J.S. The effects of a large island upon the trade-wind air stream. *Qtr. J. Roy. Meteorol. Soc.* **1955**, *81*, 538–550. [[CrossRef](#)]
9. Pearce, R.P.; Smith, R.C.; Malkus, J.S. The calculation of a sea-breeze circulation in terms of the differential heating across the coast line. *Qtr. J. Roy. Meteorol. Soc.* **1956**, *82*, 235–241. [[CrossRef](#)]
10. Jury, M.R. An inter-comparison of observational, reanalysis, satellite, and coupled model data on mean rainfall in the Caribbean. *J. Hydrometeor.* **2009**, *10*, 413–430. [[CrossRef](#)]
11. Jury, M.R.; Chiao, S. Lee-side boundary layer confluence and afternoon thunderstorms over Mayaguez, Puerto Rico. *J. Appl. Meteor. Climatol.* **2013**, *52*, 439–454. [[CrossRef](#)]
12. O'Connor, J.E.; Costa, J.E. Spatial distribution of the largest rainfall-runoff floods from basins between 2.6 and 26000 km<sup>2</sup> in the United States and Puerto Rico. *Water Resour. Res.* **2004**, *40*, W01107. [[CrossRef](#)]
13. Cooper, H.; Garstang, M.; Simpson, J. The diurnal interaction between convection and peninsular-scale forcing over south Florida. *Mon. Wea. Rev.* **1982**, *110*, 486–503. [[CrossRef](#)]
14. Blanchard, D.O.; López, R.E. Spatial patterns of convection in south Florida. *Mon. Wea. Rev.* **1985**, *113*, 1282–1299. [[CrossRef](#)]
15. Liu, C.; Moncrieff, M.W. A numerical study of the effects of ambient flow and shear on den-sity currents. *Mon. Wea. Rev.* **1996**, *124*, 2282–2303. [[CrossRef](#)]
16. Smith, R.B.; Gleason, A.C.; Gluhosky, P.A.; Grubisic, V. The wake of St. Vincent. *J. Atmos. Sci.* **1997**, *54*, 606–623. [[CrossRef](#)]
17. Carbone, R.E.; Wilson, J.W.; Keenan, T.D.; Hacker, J.M. Tropical island convection in the absence of significant topography. Part I: Life cycle of diurnally forced convection. *Mon. Wea. Rev.* **2000**, *128*, 3459–3480. [[CrossRef](#)]
18. Shepherd, J.M.; Ferrier, B.S.; Ray, P.S. Rainfall morphology in Florida convergence zones: A numerical study. *Mon. Wea. Rev.* **2001**, *129*, 177–197. [[CrossRef](#)]
19. Etlings, D. On atmospheric vortex streets in the wake of large islands. *Meteorol. Atmos. Phys.* **1989**, *41*, 157–164. [[CrossRef](#)]
20. Rasmussen, R.M.; Smolarkiewicz, P.K.; Warner, J. On the dynamics of Hawaiian cloud bands: Comparison of model results with observations and island climatology. *J. Atmos. Sci.* **1989**, *46*, 1589–1608. [[CrossRef](#)]
21. Schar, C.; Smith, R.B. Shallow-water flow past isolated topography. Part I: Vorticity production and wake formation. *J. Atmos. Sci.* **1993**, *50*, 1373–1400. [[CrossRef](#)]
22. Schar, C.; Smith, R.B. Shallow-water flow past isolated topography. Part II: Transition to vortex shedding. *J. Atmos. Sci.* **1993**, *50*, 1401–1412. [[CrossRef](#)]
23. Grubisic, V.; Smith, R.B.; Schar, C. The effect of bottom friction on shallow-water flow past an isolated obstacle. *J. Atmos. Sci.* **1995**, *52*, 1985–2005. [[CrossRef](#)]
24. Burk, S.D.; Haack, T.; Rogers, L.T.; Wagner, L.J. Island wake dynamics and wake influence on the evaporation duct and radar propagation. *J. Appl. Meteorol.* **2002**, *42*, 349–367. [[CrossRef](#)]

25. Jury, M.R. Representation of the Caribbean mean diurnal cycle in observation, reanalysis, and CMIP3 model datasets. *Theor. Appl. Climatol.* **2011**, *107*, 313–324. [[CrossRef](#)]
26. Pachauri, R.K.; Allen, M.R.; Barros, V.R.; Broome, J.; Cramer, W.; Christ, R.; Church, J.A.; Clarke, L.; Dahe, Q.; Dasgupta, P.; et al. *Climate Change Synthesis Report; Contribution of Working Group-I to 5th Assessment Report*; Pachauri, R.K., Meyer, L., Eds.; World Meteorological Organization: Geneva, Switzerland, 2014; p. 151.
27. Reyer, C.; Adams, S.; Albrecht, T.; Baarsch, F.; Boit, A.; Trujillo, N.C.; Cartsburg, M.; Coumou, D.; Eden, A.; Fernandes, E.; et al. Climate change impacts in Latin America and the Caribbean and their implications for development. *Reg. Environ. Change* **2017**, *17*, 1601–1621. [[CrossRef](#)]
28. Kendon, E.; Roberts, N.; Fowler, H.; Roberts, M.; Chan, S.; Senior, C. Heavier summer downpours with climate change revealed by weather forecast resolution model. *Nat. Clim. Change* **2014**, *4*, 570–576. [[CrossRef](#)]
29. Prein, A.F.; Liu, C.; Ikeda, K.; Trier, S.B.; Rasmussen, R.M.; Holland, G.J.; Clark, M.P. Increased rainfall volume from future convective storms in the US. *Nat. Clim. Change* **2017**, *7*, 880–884. [[CrossRef](#)]
30. Rasmussen, K.L.; Prein, A.F.; Rasmussen, R.M.; Ikeda, K.; Liu, C. Changes in the convective population and thermodynamic environments in convection-permitting regional climate simulations over the United States. *Climate Dyn.* **2020**, *55*, 383–408. [[CrossRef](#)]
31. Gould, W.A.; Diaz, E.L.; Álvarez-Berrios, N.L.; Aponte-González, F.; Archibald, W.; Bowden, J.H.; Carrubba, L.; Crespo, W.; Fain, S.J.; González, G.; et al. *US Caribbean, in Impacts, Risks and Adaptation in the United States: 4th National Climate Assessment*; Reidmiller, D., Avery, C.W., Easterling, D.R., Kunkel, K.E., Lewis, K.L.M., Maycock, T.K., Stewart, B.C., Eds.; US Global Change Research Program: Washington, DC, USA, 2018; Volume 2, pp. 809–871. [[CrossRef](#)]
32. Funk, C.C.; Peterson, P.J.; Landsfeld, M.F.; Pedreros, D.H.; Verdin, J.P.; Rowland, J.D.; Romero, B.E.; Husak, G.J.; Michaelsen, J.C.; Verdin, A.P. A quasi-global precipitation time series for drought monitoring. *US Geological. Surv. Data Ser.* **2014**, *832*, 1–4. [[CrossRef](#)]
33. Eyring, V.; Bony, S.; Meehl, G.A.; Senior, C.A.; Stevens, B.; Stouffer, R.J.; Taylor, K.E. Overview of the Coupled Model Intercomparison Project Phase 6 (CMIP6) experimental design and organization. *Geosci. Model Dev.* **2016**, *9*, 1937–1958. [[CrossRef](#)]
34. Joyce, R.J.; Janowiak, J.E.; Arkin, P.A.; Xie, P. cMORPH: A method that produces global precipitation estimates from passive microwave and infrared data at high spatial and temporal resolution. *J. Hydrometeor.* **2004**, *5*, 487–503. [[CrossRef](#)]
35. Harris, I.; Jones, P.D.; Osborn, T.J.; Lister, D.H. Updated high resolution grids of monthly climatic observations—the CRU Dataset. *Int. J. Climatol.* **2014**, *34*, 623–642. [[CrossRef](#)]
36. Dee, D.P.; Uppala, S.M.; Simmons, A.J.; Berrisford, P.; Poli, P.; Kobayashi, S.; Andrae, U.; Balmaseda, M.A.; Balsamo, G.; Bauer, P.; et al. The ERA-Interim reanalysis: Configuration and performance of the data assimilation system. *Qtr. J. Roy. Meteorol. Soc.* **2011**, *13*, 553–597. [[CrossRef](#)]
37. Poli, P.; Hersbach, H.; Dee, D.P.; Berrisford, P.; Simmons, A.J.; Vitart, F.; Laloyaux, P.; Tan, D.G.H.; Peubey, C.; Thépaut, J.-N.; et al. ERA-20C: An atmospheric reanalysis of the twentieth century. *J. Climate* **2016**, *29*, 4083–4097. [[CrossRef](#)]
38. Rodell, M.; Houser, P.R.; Jambor, U.; Gottschalck, J.; Mitchell, K.; Meng, C.-J.; Arsenault, K.; Cosgrove, B.; Radakovich, J.; Bosilovich, M.; et al. The Global Land Data Assimilation System. *Bull. Amer. Meteor. Soc.* **2004**, *85*, 381–394. [[CrossRef](#)]
39. McNally, A.; Arsenault, K.; Kumar, S.; Shukla, S.; Peterson, P.; Wang, S.; Funk, C.; Peters-Lidard, C.D.; Verdin, J.P. A land data assimilation system for sub-Saharan Africa food and water security applications. *Sci. Data* **2017**, *4*, 170012. [[CrossRef](#)] [[PubMed](#)]
40. Schneider, U.; Becker, A.; Finger, P.; Meyer-Christoffer, A.; Rudolf, B.; Ziese, M. *GPCC Full Data Monthly Product Version 8 at 0.5°: Monthly Land-Surface Precipitation from Rain-Gauges Built on GTS-based and Historical Data*; GPCC: Offenbach, Germany, 2018.
41. Huffman, G.J.; Adler, R.F.; Morrissey, M.M.; Bolvin, D.T.; Curtis, S.; Joyce, R.; McGavock, B.; Susskind, J. Global precipitation at one-degree daily resolution from multi-satellite observations. *J. Hydrometeor.* **2001**, *2*, 36–50. [[CrossRef](#)]
42. Huffman, G.J.; Adler, R.F.; Bolvin, D.T.; Gu, G.; Nelkin, E.J.; Bowman, K.P.; Hong, Y.; Stocker, E.F.; Wolff, D.B. The TRMM Multi-satellite Precipitation Analysis (TMPA): Quasi-global, multiyear, combined-sensor precipitation estimates at fine scales. *J. Hydrometeor.* **2007**, *8*, 38–55. [[CrossRef](#)]

43. Hou, A.Y.; Kakar, R.K.; Neeck, S.; Azarbarzin, A.A.; Kummerow, C.D.; Kojima, M.; Oki, R.; Nakamura, K.; Iguchi, T. The Global Precipitation Measurement mission. *Bull. Amer. Meteor. Soc.* **2014**, *95*, 701–722. [[CrossRef](#)]
44. Ghiggi, G.; Humphrey, V.; Seneviratne, S.I.; Gudmundsson, L. GRUN: An observation-based global gridded runoff dataset from 1902 to 2014. *Earth Syst. Sci. Data* **2019**, *11*, 1655–1674. [[CrossRef](#)]
45. Chassignet, E.P.; Hurlburt, H.E.; Metzger, E.J.; Smedstad, O.M.; Cummings, J.A.; Halliwell, G.R.; Bleck, R.; Baraille, R.; Wallcraft, A.J.; Lozano, C.; et al. US GODAE: Global ocean prediction with the Hybrid coordinate ocean model (HYCOM). *Oceanography* **2009**, *22*, 64–75. [[CrossRef](#)]
46. Frieler, K.; Lange, S.; Piontek, F.; Reyer, C.P.; Schewe, J.; Warszawski, L.; Zhao, F.; Chini, L.; Denvil, S.; Emanuel, K. Assessing the impacts of 1.5°C global warming—Simulation protocol of the Inter-Sectoral Impact Model Intercomparison Project ISIMIP2b. *Geosci. Model Dev.* **2018**, *10*, 4321–4345. [[CrossRef](#)]
47. Pinzon, J.E.; Tucker, C.J. A non-stationary 1981–2012 AVHRR NDVI3g time series. *Remote Sens.* **2014**, *6*, 6929–6960. [[CrossRef](#)]
48. Kanamitsu, M.; Ebisuzaki, W.; Woolen, J.; Yang, S.K.; Hnilo, J.J.; Fiorino, M.; Potter, G.L. NCEP-2 reanalysis. *Bull. Amer. Meteorol. Soc.* **2002**, *83*, 1631–1643. [[CrossRef](#)]
49. Reynolds, R.W.; Smith, T.M.; Liu, C.; Chelton, D.B.; Casey, K.S.; Schlax, M.G. Daily high-resolution blended analyses for sea surface temperature. *J. Climate* **2007**, *20*, 5473–5496. [[CrossRef](#)]
50. Lee, H.-T.; Gruber, A.; Ellingson, R.G.; Laszlo, I. Development of the HIRS outgoing longwave radiation climate dataset. *J. Atmos. Ocean Tech.* **2007**, *24*, 2029–2047. [[CrossRef](#)]
51. Carton, J.A.; Chepurin, G.A.; Chen, L. SODA-3 a new ocean climate reanalysis. *J. Climate* **2018**, *31*, 6967–6983. [[CrossRef](#)]
52. Fenton, J.D.; Keller, R.D. The calculation of streamflow from measurements of stage, Tech Rep 1-6, CRC hydrology, CRC hydrology. 2001. Available online: <http://johndfenton.com/Papers/Calculation-of-streamflow-from-measurements-of-stage.pdf> (accessed on 5 November 2020).
53. Legates, D.R.; McCabe, G.J. Evaluating the use of ‘goodness-of-fit’ measures in hydrologic and hydroclimatic model validation. *Water Resour. Res.* **1999**, *35*, 233–241. [[CrossRef](#)]
54. Nigam, S.; Sengupta, A.; Ruiz-Barradas, A. Atlantic–Pacific links in observed multidecadal SST variability: Is the Atlantic Multidecadal Oscillation’s phase reversal orchestrated by the Pacific Decadal Oscillation? *J. Climate* **2020**, *33*, 5479–5505. [[CrossRef](#)]
55. Allen, M.R.; Ingram, W.J. Constraints on future changes in climate and the hydrologic cycle. *Nature* **2002**, *491*, 228–232. [[CrossRef](#)] [[PubMed](#)]
56. DeJong, R.; de Bruin, S.; de Wit, A.; Schaepman, M.E.; Dent, D.L. Analysis of mono-tonic greening and browning trends from global NDVI time-series. *Remote Sens. Environ.* **2011**, *115*, 692–702. [[CrossRef](#)]
57. Gamble, D.W.; Parnel, D.B.; Curtis, S. Spatial variability of the Caribbean mid-summer drought and relation to the north Atlantic high. *Int. J. Climatol.* **2008**, *28*, 343350. [[CrossRef](#)]
58. Hall, T.; Sealy, A.; Stephenson, T.; Kusunoki, S.; Taylor, M.; Chen, A.; Kitoh, A. Future climate of the Caribbean from a super-high-resolution atmospheric general circulation model. *Theor. Appl. Climatol.* **2012**, *113*. [[CrossRef](#)]
59. Jury, M.R.; Winter, A. Warming of an elevated layer over the Caribbean. *Clim. Change* **2009**. [[CrossRef](#)]

**Publisher’s Note:** MDPI stays neutral with regard to jurisdictional claims in published maps and institutional affiliations.



© 2020 by the author. Licensee MDPI, Basel, Switzerland. This article is an open access article distributed under the terms and conditions of the Creative Commons Attribution (CC BY) license (<http://creativecommons.org/licenses/by/4.0/>).